RSC Advances

PAPER

View Article Online
View Journal | View Issue

Check for updates

Cite this: *RSC Adv.*, 2025, **15**, 37660

Oxidation-free nanoscale optomechanical sensor incorporating a triangular truss resonator for crosstalk-free bimodal pressure and temperature sensing

Abdullah Taharat, * Mohammad Abrar Kabir, Aseer Imad Keats, A. K. M. Rakib and Rakibul Hasan Sagor

Recently, we have witnessed significant advancements made by researchers in using silver-based Metal–Insulator–Metal (MIM) plasmonic devices for their improved performance. However, the practical applicability of these sensors is still under scrutiny. Very few studies have been conducted looking for alternative approaches to improve the viability of deploying these sensors for use in challenging operational conditions. This paper articulates a novel MIM-based dual-function optomechanical sensor utilizing oxidation-free gold as the plasmonic material, capable of sensing pressure and temperature in parallel. To the best of the authors' knowledge, this marks the first instance of investigating an optical MIM pressure sensor using oxidation-resistant gold as the plasmonic material. The proposed sensor consists of a Triangular Truss Resonator (TTR) and a pair of Rectangular Cavities (RCs) coupled to a straight waveguide. The TTR is utilized for sensing pressure, while the RCs are responsible for detecting temperature variations. Employing the Finite Element Method (FEM), we numerically investigated the device's transmission spectrum, which comprised two independent resonant wavelengths, namely mode 1 and mode 2, enabling dual-function sensing capabilities with distinct and independent responses. The sensor demonstrates a notable pressure sensitivity of 77.1 nm MPa^{-1}, along with a temperature sensitivity of 0.488 nm $°C^{-1}$. Its impressive performance metrics, coupled with the use of oxidation-resistant gold, not only ensure enhanced performance and stability of the sensor but also offer a significantly extended operational lifespan. These traits highlight the sensor's potential for real-world applications in diverse scenarios, positioning it as a compelling candidate for substituting oxidation-prone silver and finding its use in real-world innovative optomechanical sensing platforms.

Received 1st July 2025
Accepted 10th September 2025

DOI: 10.1039/d5ra04668h

rsc.li/rsc-advances

Open Access Article. Published on 09 October 2025. Downloaded on 1/29/2026 1:22:41 PM.
This article is licensed under a Creative Commons Attribution-NonCommercial 3.0 Unported Licence.

1 Introduction

Surface Plasmon Polaritons (SPPs), which are transverse electromagnetic (EM) waves propagating along a metal–dielectric interface, have driven the evolution of the field of nanophotonics fundamentally by circumventing the diffraction limit of light and enabling its confinement at subwavelength scales.[1,2] SPPs are generated at the metal–dielectric junction due to the coupling of incident photons and oscillating free electrons at specific resonant wavelengths.[3] The unique features of SPPs, encompassing strong light–matter interactions and manipulation of light at nanoscale dimensions, have facilitated the design and development of a multitude of miniaturized optical devices able to function independently.[4] The ever-expanding list of devices, either investigated practically or through simulations, includes demultiplexers,[5] refractive index (RI) sensors,[6–8] filters,[9] Mach–Zehnder interferometers (MZIs),[10] *etc.*

The field of optomechanical sensing has recently witnessed promising research based on leveraging the potential of SPPs for sensing fluid pressure. Optomechanical sensors exploit the interaction between incident light and mechanical deformation caused by the applied pressure, while also avoiding the restrictions posed by traditional pressure sensors. They can work flawlessly under extreme conditions that involve exposure to EM interference and have compact sizes.[11,12] Among the various waveguide configurations used for generating SPPs, Metal–Insulator–Metal (MIM)-based plasmonic nanometallic structures have gained significant attention because of their ability to guide light with high EM field confinement, short response time and low optical losses.[13,14] In 2015, Wu *et al.* proposed a MIM optical pressure sensor consisting of an H-shaped resonator that utilized silver as the plasmonic material.[15] Consequently, numerous studies have been conducted in this domain, where researchers mostly focused on improving

Department of Electrical and Electronic Engineering, Islamic University of Technology (IUT), Gazipur-1704, Bangladesh. E-mail: abdullahtaharat@iut-dhaka.edu

© 2025 The Author(s). Published by the Royal Society of Chemistry

Open Access Article. Published on 09 October 2025. Downloaded on 1/29/2026 1:22:41 PM. This article is licensed under a Creative Commons Attribution-NonCommercial 3.0 Unported Licence.

the performance of the sensor by varying its structural design. Tathfif *et al.* presented a novel optical pressure sensor incorporating arrays of silver nanorods into a ladder-shaped resonator, which demonstrated a sensitivity of 25.4 nm MPa^{-1}.[16] Ma *et al.* investigated the impact of adding baffles to the resonator in a bid to improve the sensitivity of optical pressure sensors. They achieved a threefold increase in sensitivity after the addition of a silver baffle to the sensor structure.[17] While the majority of research in this domain has primarily focused on sensing a single parameter, such as pressure, there is an emerging trend towards multi-modal sensing. Optical-fiber-based sensors have mostly been studied for multiparameter sensing. Although this category of sensors offers high sensing performance, their structural dimensions limit their applicability in scenarios requiring compact devices. In contrast, MIM devices usher in a new paradigm in the arena of miniaturized sensing platforms.

Going through the existing works on MIM optical pressure sensors, we observed that, besides the lack of multifunctional sensing platforms, very little effort has been made in the search for novel materials to replace silver as the plasmonic material in optical pressure sensors. Silver as a plasmonic material suffers from numerous drawbacks, one of which is the problem of oxidation when exposed to moisture or air, as a result of which irregularly distributed clumps of silver sulfide develop on the metal surface. The formation of such a compound heavily degrades silver's chemical and plasmonic properties.[18] Heavily doped silicon has been studied of late, which could mitigate this problem to some extent, considering that silicon forms a protective layer of silicon dioxide upon exposure to air.[11] However, it is not a suitable choice for long-term use, especially in applications requiring extended operational stability and durability.

In this paper, we propose a novel optical pressure sensor where gold is preferred over other traditional plasmonic materials, taking into account its strong oxidation resistance and stability under varying conditions. Our design incorporates a Triangular Truss Resonator (TTR) and a couple of Rectangular Cavities (RCs), which are coupled with a straight MIM waveguide. To the best of our knowledge, this study marks the first instance of using oxidation-resistant gold in the design of an optical MIM pressure sensor. Moreover, the presence of RCs enables us to simultaneously detect multiple physical parameters independently, such as pressure and temperature, using a single platform. The designed sensor, being capable of performing dual-sensing, attains pressure and temperature sensitivity of 77.1 nm MPa^{-1} and 0.488 nm $°C^{-1}$, respectively. Alongside its superior performance, the sensor's robustness and stability underscore its potential for use in advanced real-world scenarios.

2 Structural model and simulation setup

The proposed sensor features a straight MIM waveguide coupled with a triangular truss resonator and a pair of rectangular cavities. Fig. 1 illustrates the top view of the sensor structure in 2D space. The waveguide and the resonator cavities are filled with air, while the bottom-left cavity is sealed with polydimethylsiloxane (PDMS) for temperature sensing. The remaining part consists of gold, marked in emerald color. The structural parameters are detailed in Table 1. The design is optimized for dual-parameter sensing, enabling simultaneous pressure and temperature detection without significant cross-sensitivity.

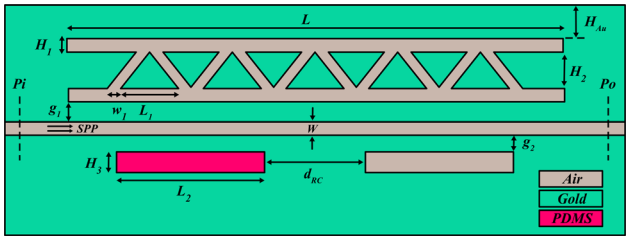

Fig. 1 2D layout of the designed sensor.

Gold (Au) is chosen as the metallic component due to its excellent chemical stability and strong plasmonic response. The frequency-dependent permittivity of gold is modeled using data from Johnson *et al.*'s research, which provides experimentally validated optical constants.[19] The Drude model defines the permittivity of gold as:[20]

$$\varepsilon_{\mathrm{Au}}(\omega) = \varepsilon_{\infty} - \frac{{\omega_p}^2}{\omega^2 + \mathrm{i}\omega\Gamma} \quad (1)$$

where ω_{p} is the plasma frequency, Γ is the damping constant, and ε_{∞} represents the high-frequency permittivity limit.

The real part of the permittivity $\mathrm{Re}(\varepsilon_{\mathrm{Au}})$ and the imaginary part $\mathrm{Im}(\varepsilon_{\mathrm{Au}})$ are plotted in Fig. 2(a), while the corresponding refractive index (n) and extinction coefficient (k) are shown in Fig. 2(b).

COMSOL Multiphysics software was utilized to numerically solve the sensor's related EM wave equations using the Finite Element Method (FEM) and employing triangular meshing. Scattering boundary conditions were set around the metal edges to absorb the outgoing waves and eliminate internal wave

Table 1 Geometric parameters of the proposed sensor

Parameters	Notation	Value (nm)
Height of the horizontal slot of the TTR	H_1	33
Gap between horizontal slots of the TTR	H_2	88
Height of the RC	H_3	50
Thickness of the top gold layer	H_{Au}	100
Gap between the TTR and waveguide	g_1	28
Gap between the RC and waveguide	g_2	30
Length of the triangular truss	L_1	140
Length of the RC	L_2	358
Length of the horizontal slot of the TTR	L	1200
Distance between the two RCs	d_{RC}	244
Width of the triangular truss	w_1	32.5
Width of the straight waveguide	W	32

© 2025 The Author(s). Published by the Royal Society of Chemistry

Open Access Article. Published on 09 October 2025. Downloaded on 1/29/2026 1:22:41 PM.
This article is licensed under a Creative Commons Attribution-NonCommercial 3.0 Unported Licence.

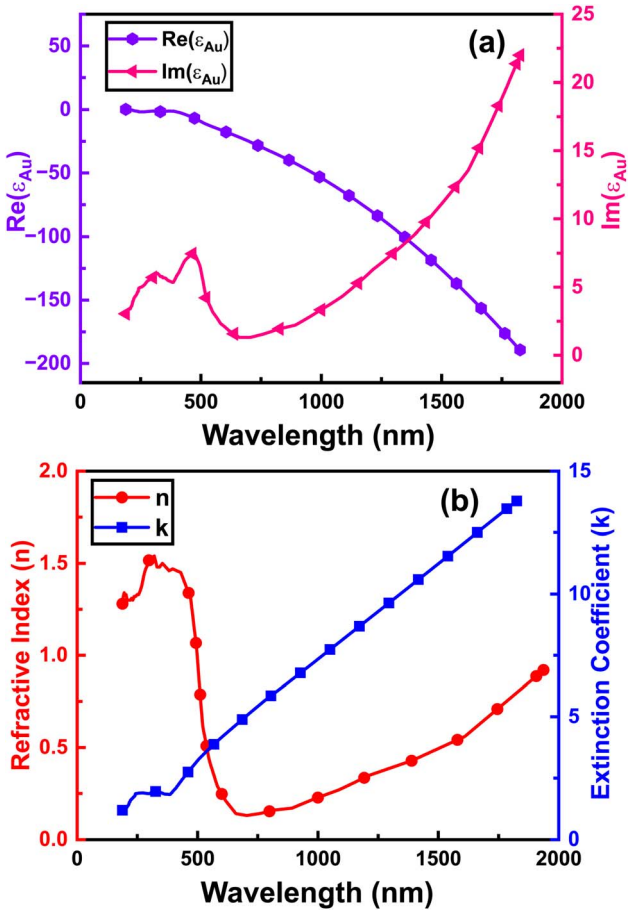

Fig. 2 (a) Real and imaginary parts of gold's permittivity. (b) Refractive index and extinction coefficient of gold.

reflections within the sensor. Simulations were conducted in 2D to ensure faster computational speed. During fabrication, it has been reported that designs exceeding a height threshold of 800 nm replicate the simulation results obtained in 2D. This acts as a benchmark to provide an accurate representation of 3D conditions, validating the accuracy and practical applicability of our simulation approach.[21]

To further justify the use of 2D investigation, we performed a 3D simulation of our proposed structure, where we varied its height over the range of 45 nm to 1000 nm at a wavelength of 1550 nm. The real part of the effective refractive index, Re(n_{eff}), was determined for different heights, as shown in Fig. 3. The value of Re(n_{eff}) plays a significant role in defining the resonant wavelength of the structure. As the SPPs traverse along the straight MIM waveguide, a fraction of the evanescent field leaks into the resonator, coupling with the resonator cavity. After propagating along the effective length of the cavity, it re-couples back to the waveguide. This creates a standing wave resonance at specific wavelengths, termed the resonant wavelength. According to standing wave theory, the resonance condition requires the wavelength (λ_{res}) to satisfy:[22]

$$\lambda_{\text{res}} = \frac{2\text{Re}(n_{\text{eff}})L}{m - \psi_r/\pi}, \quad (m = 1, 2, \ldots) \tag{2}$$

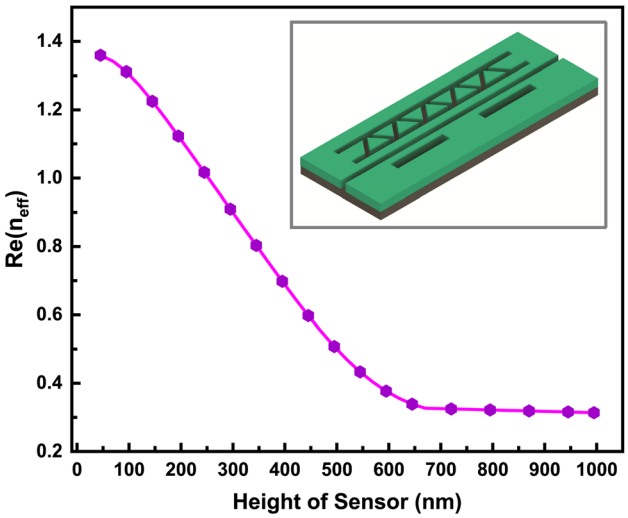

Fig. 3 Variation of the real part of the effective refractive index (Re(n_{eff})) with the height of the 3D simulated structure, indicating the quasi-2D behavior.

where m is the order of the resonant mode, L is the effective length of the resonant cavity, and ψ_r represents the phase shift upon reflection at the cavity boundaries. The exact value of ψ_r due to reflection at metal–dielectric interfaces depends on the cavity geometry, metal film thickness, and refractive-index mismatch at the interfaces.[23] In our numerical analysis, the FEM solver inherently accounts for the reflection-induced phase shift corresponding to the given geometry.

It follows from this equation that variations in structural parameters and dielectric refractive index significantly influence the resonance wavelength. Since λ_{res} directly depends on Re(n_{eff}), a convergence of Re(n_{eff}) with increasing height of the structure would signify that the resonant wavelength is effectively insensitive to further increases in height.

It is observed from Fig. 3 that the Re(n_{eff}) stabilizes for structure heights above approximately 700 nm. This observation reveals that the mode confinement in the vertical direction no longer changes significantly, and the structure behaves as quasi-2D. Hence, when the Re(n_{eff}) becomes constant, the resonant wavelength predicted by a 2D model (which assumes an infinite height) will closely match the 3D value. Thus, for heights above this threshold, 2D simulations are justified and they accurately capture resonance behavior while avoiding the higher computational cost of full 3D simulations.

Ports Pi and Po in Fig. 1 serve as the input and output for the transverse magnetic (TM) polarized light, respectively. The dispersion relation for an SPP mode in a MIM waveguide is given by:[24]

$$\tanh\left(\frac{k_1 \times W}{2}\right) = -\frac{\varepsilon_{\text{air}} \times k_2}{\varepsilon_{\text{Au}} \times k_1} \tag{3}$$

where k_1 and k_2 are the wave vectors in the air and metal layers, respectively, defined as:

$$k_1{}^2 = \beta^2 - \varepsilon_{\text{air}} \times k_0{}^2 \tag{4}$$

© 2025 The Author(s). Published by the Royal Society of Chemistry

Open Access Article. Published on 09 October 2025. Downloaded on 1/29/2026 1:22:41 PM.
This article is licensed under a Creative Commons Attribution-NonCommercial 3.0 Unported Licence.

$$k_2^2 = \beta^2 - \varepsilon_{Au} \times k_0^2 \quad (5)$$

Here, $k_0 = \frac{2\pi}{\lambda_0}$ represents the wave number of light in a vacuum, and λ_0 is the wavelength of the incident light. The propagation constant of the MIM waveguide is given by $\beta = n_{eff} \times k_0$, where n_{eff} is the effective refractive index.

3 Result evaluation and discussion

The transmission spectrum of the proposed sensor structure at room temperature (20 °C) and under no applied pressure (0 MPa) is shown in Fig. 4. It exhibits two distinct resonant modes, mode 1 and mode 2, at wavelengths λ_{res} = 1562.9 nm and 1712.2 nm, respectively. Mode 1 appears because of the coupling between the lower rectangular cavities and the straight waveguide, while the coupling involving the upper triangular truss resonator gives rise to mode 2. To further comprehend the resonance within the proposed structure, we analyzed the electric field distributions, $|E| = (E_x^2 + E_y^2)^{1/2}$, and magnetic field distributions, $|H| = (H_z^2)^{1/2}$, at λ_{res} for mode 1 and mode 2. The *E*-fields and *H*-fields are illustrated in Fig. 5 and 6, respectively. At mode 1, the fields are predominantly confined within the left rectangular cavity (LRC) below the waveguide, which indicates this cavity's strong influence at mode 1. In contrast, in mode 2, the fields are concentrated in the triangular truss resonator. This indicates that when pressure is applied to the structure from top, it will deform the triangular truss resonator, resulting in a shift in λ_{res} at mode 2, while any variation in the temperature of the PDMS will cause a shift in the λ_{res} at mode 1.

3.1 Pressure sensing

In the proposed gold-based plasmonic pressure sensor, applied pressure deforms the resonator along with the sensor's top surface, altering its effective volume and subsequently shifting the resonant wavelength. This behavior follows Slater's law:[25]

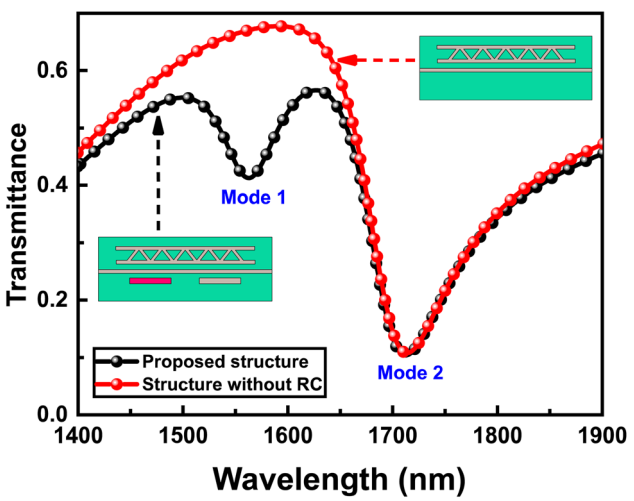

Fig. 4 Transmission spectra for different structures of the sensor. The black graph represents the results for the proposed sensor and the red graph represents the spectrum for the structure without RCs.

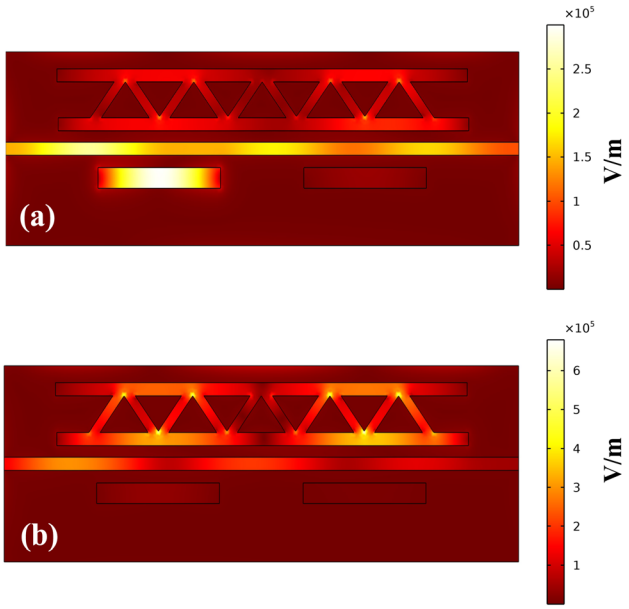

Fig. 5 *E*-field at (a) λ_{res} = 1562.9 nm (mode 1), (b) λ_{res} = 1712.2 nm (mode 2).

$$\frac{\delta f}{f} = -\frac{(\varepsilon_0 E^2 - \mu_0 H^2)\delta V}{\int_V (\varepsilon_0 E^2 + \mu_0 H^2)\delta V} \quad (6)$$

where f is the resonant frequency, V is the volume of the resonator, E and H represent the intensities of the electric and magnetic fields, and ε_0 and μ_0 are the free space's permittivity and permeability, respectively. This law indicates that when the magnetic field dominates, the resonant wavelength undergoes a redshift, and when the electric field dominates, a blueshift will occur as a result of the deformation of the resonator.[25]

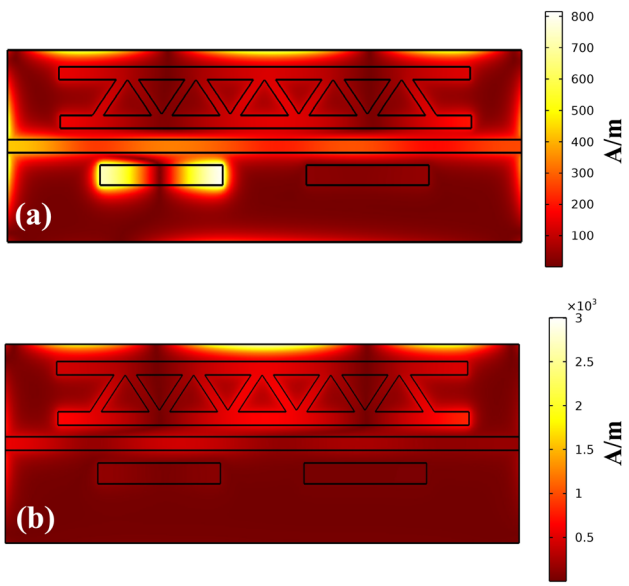

Fig. 6 *H*-field at (a) λ_{res} = 1562.9 nm (mode 1), (b) λ_{res} = 1712.2 nm (mode 2).

Open Access Article. Published on 09 October 2025. Downloaded on 1/29/2026 1:22:41 PM. This article is licensed under a Creative Commons Attribution-NonCommercial 3.0 Unported Licence.

Slater's law forms the basis for sensing pressure changes through monitoring wavelength shifts during SPP interactions. As discussed in Section 2, variation in the structural parameters of the designed sensor influences the value of Re(n_{eff}) and thus the resonant wavelength. When the resonator structure deforms under applied pressure, its geometry changes, leading to a variation in Re(n_{eff}). Consequently, in our simulations, Re(n_{eff}) was recalculated dynamically for each deformation state to account for the pressure-induced changes.

To explore how the designed sensor behaves, we vary the pressure from 0.27 MPa to 0.80 MPa at a constant temperature of 20 °C, which corresponds to increasing the deformation (d) of the top layer of TTR from $d = 4$ nm to $d = 12$ nm, in steps of 2 nm. A circular arc emerges due to the deformation, as shown in Fig. 7,[11] and its radius (R) is determined by eqn (7).

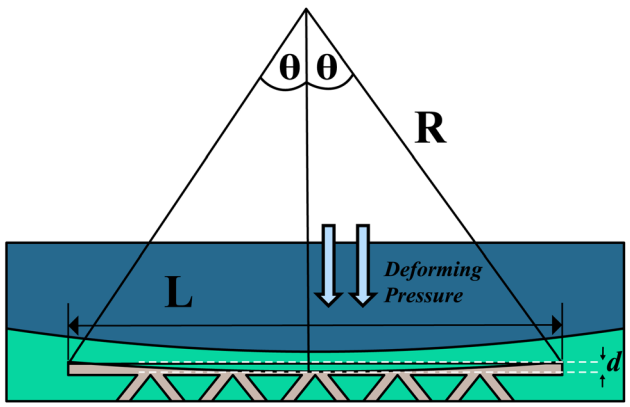

Fig. 7 Formation of an arc in the resonator with a deformation (d) due to the exerted pressure.

$$R = \frac{L^2 + 4d^2}{8d} \tag{7}$$

The electric and magnetic field distributions at the resonant modes after deformation ($d = 12$ nm) of the structure are illustrated in Fig. 8. It can be observed that it exhibits the same confinement characteristics as the initial structure for mode 1 and mode 2 (Fig. 5 and 6). Mode 1 continues to be strongly localized in the LRC, while mode 2 remains concentrated in the TTR. The absence of mode hybridization or significant distortion of the field pattern confirms our earlier conclusion that pressure sensing is dominated by mode 2 and temperature sensing by mode 1, thereby ensuring robust dual-parameter sensing.

The applied pressure is calculated from the deformation using the following equation:[16]

$$P = \frac{2Y_{\text{Au}}H_{\text{Au}}{}^3 d}{L^4} \tag{8}$$

where P is the exerted pressure on the sensor structure, Y_{Au} is the Young's modulus of gold, having a value of 69.1 GPa,[26] H_{Au} is the thickness of the top gold film, and L is the length of the TTR where pressure is exerted. It is shown in Fig. 9(a and b) that mode 2 experiences a significant redshift when the applied pressure increases. This incident indicates the outcome of Slater's law, as the applied pressure deforms the resonator cavity, which leads to a reduction of the resonator's volume and a significant redshift of approximately 10 nm per 0.13 MPa change in pressure. In contrast, examining the change in the resonant response of mode 1 (temperature-sensitive mode) under varying applied pressure in Fig. 9(c), we observe that its

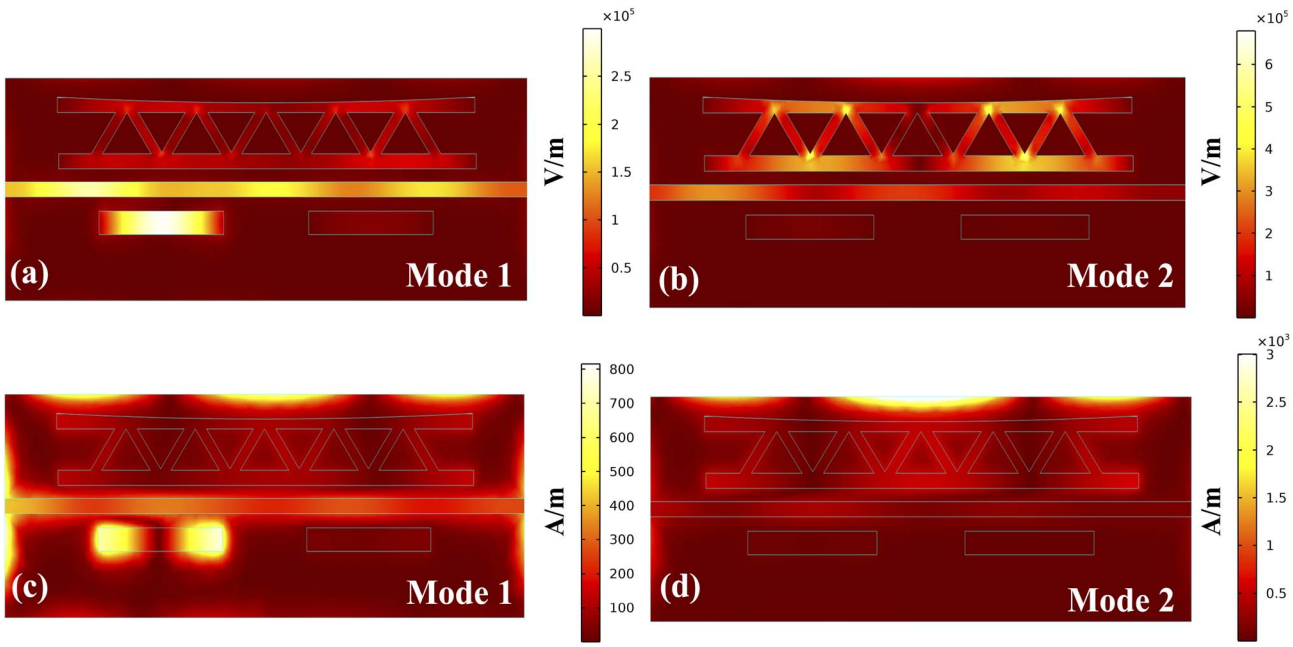

Fig. 8 (a) E-field at mode 1 after deformation. (b) E-field at mode 2 after deformation. (c) H-field at mode 1 after deformation. (d) H-field at mode 2 after deformation.

© 2025 The Author(s). Published by the Royal Society of Chemistry

Open Access Article. Published on 09 October 2025. Downloaded on 1/29/2026 1:22:41 PM.
This article is licensed under a Creative Commons Attribution-NonCommercial 3.0 Unported Licence.

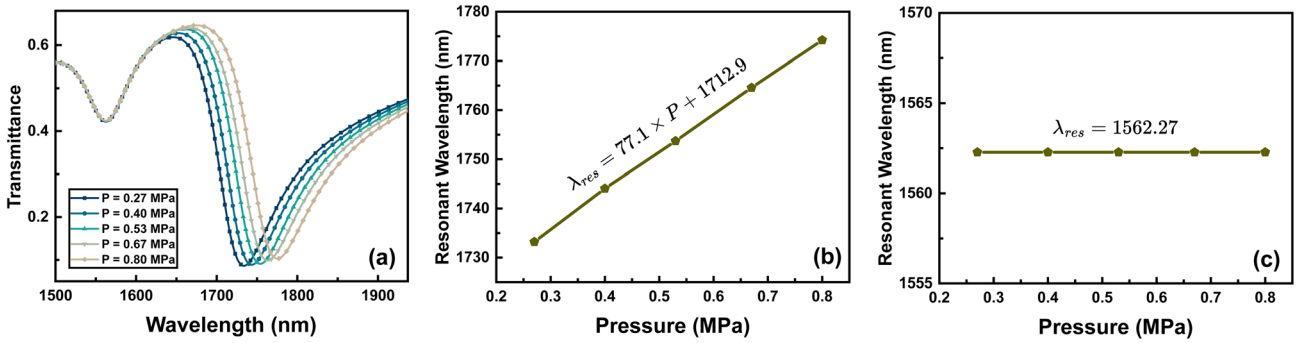

Fig. 9 (a) Transmittance profile of the proposed sensor under varying applied pressure. (b) Graph of the resonant wavelength *versus* pressure for mode 2. (c) Graph of resonant wavelength *versus* pressure for mode 1.

resonant wavelength remains effectively unchanged at 1562.27 nm when the pressure is varied, confirming that pressure fluctuations do not influence its spectral position. This result demonstrates the isolation of sensing channels and reinforces the claim of crosstalk-free performance of our dual sensing device.

The pressure sensitivity (S_P) of the sensor is measured using the following equation:[16]

$$S_P = \frac{\Delta\lambda_{res}}{\Delta P} \quad (9)$$

Here, λ_{res} is the shift of resonant wavelength, and ΔP indicates the change of pressure. The sensitivity obtained from our designed sensor is 77.1 nm MPa^{-1}. Furthermore, Fig. 9(b) illustrates the relationship between resonant wavelength and applied pressure; the result of this analysis shows a linear relationship. This linearity facilitates the precise detection of pressure shifts. Even minute changes in pressure, and hence, the resonant wavelength, can easily be identified using an Optical Spectrum Analyzer (OSA) with high accuracy, eliminating any potential complexity.

The pressure detection limit, defined as the smallest change in pressure that the sensor can precisely detect, depends on the resolution of the OSA. The expression for determining the pressure detection limit (DL_P) of the sensor can be written as the ratio of the smallest wavelength shift that can be perceived using the OSA to the sensor's pressure sensitivity:[27]

$$DL_P = \frac{\Delta\lambda_{min}}{S_P} \quad (10)$$

where $\Delta\lambda_{min}$ is the minimum detectable wavelength shift (set by the OSA resolution). In this work, we have considered the value of $\Delta\lambda_{min}$ to be 0.001 nm, corresponding to the typical resolution of commercial spectrum analyzers.[28] Using the measured pressure sensitivity, the limit of the detection of pressure of the proposed sensor is calculated to be 1.30×10^{-5} MPa. This high resolution ensures that even extremely small pressure variations can be reliably measured, enabling precise monitoring and accurate measurements in sensitive applications.

While Slater's law provides a direct relation between deformation volume and resonance wavelength shift, it inherently assumes an ideal deformation. Practically, the deformation of the resonator structure may have small deviations from the ideal value. To evaluate the robustness of Slater's law under practical conditions, we introduced controlled perturbations in the deformation (±1% and ±1.5%) and investigated the effect of such uncertainties on the calculated pressure sensitivity. The results obtained are summarized in Table 2. The table shows that the change in pressure sensitivity of the device is very low and remains within approximately ∼±1%. This indicates that the impact of such uncertainties on the device performance in a real-world setting is negligible for the proposed sensor, and thus validates the practical implication of Slater's law in our study.

Furthermore, to determine the durability of the TTR under repeated pressure cycling, we have assessed the mechanical behavior of the gold structure. Our analysis indicates that the applied pressures (up to 0.80 MPa, corresponding to 12 nm deformation on a 1200 nm span) operate well within the elastic regime of gold thin films, with no expected plastic deformation or significant fatigue over typical cycle counts.

The thickness of the top gold layer, which is being deformed due to the applied pressure, is taken as 100 nm in our design; such a small thickness is known to promote elastic deformation. Baek *et al.* conducted an experimental investigation into the effect of varying the thickness of gold films on their mechanical properties.[29] The results exhibited an inverse relation between the thickness of the gold film and the yield strength, where a reduction in the film thickness resulted in an increase in its yield stress. Moreover, the maximum bending stresses acting upon the thin gold layer corresponding to the range of values of deformation utilized in our analysis fall well below the yield strength of nanostructured gold thin films,

Table 2 Effect of error in deformation on the pressure sensitivity relative to the nominal sensitivity of the proposed sensor

Error in deformation, d	Pressure sensitivity (nm MPa^{-1})	Change in pressure sensitivity
+1%	77.82	+0.934%
−1%	76.15	−1.23%
+1.5%	77.89	+1.02%
−1.5%	76.15	−1.23%

Open Access Article. Published on 09 October 2025. Downloaded on 1/29/2026 1:22:41 PM. This article is licensed under a Creative Commons Attribution-NonCommercial 3.0 Unported Licence.

further ensuring elastic deformation of the TTR without plasticity.[29]

The long-term reliability of the thin gold layer under repeated cycling of applied pressure must also be considered. In this regard, fatigue testing of gold films, supported on Si_xN_y substrates, has demonstrated their ability to withstand >10 000 pressure cycles without exhibiting structural failure.[30] The gold nanostructures retained their structural integrity, with only minor residual stress variations observed. This finding provides strong experimental evidence that the gold nanolayer in our design, being supported by an underlying substrate, can sustain repeated cycling of pressure while maintaining elastic behavior and avoiding fatigue-induced fracture. Therefore, within the operational deformation range and repeated cycling, the TTR is expected to retain its elastic response, without the appearance of plastic deformation or fatigue-related damage of the gold layer.

3.2 Temperature sensing

A multiprocessor system-on-chip (MPSoC) is a type of system-on-chip (SoC) architecture that contains multiple instruction-set processors and has emerged as a powerful modern technology. To ensure that MPSoCs perform reliably and optimally in complex environments, one critical aspect that should be considered is to monitor their temperature fluctuations closely.[31] The existence of independent dual peaks in our proposed optical sensor makes it ideal for integration into such sophisticated devices and carrying out such tasks. For monitoring changes in temperature, the proposed structure relies on the temperature-sensitive material filling the LRC. The thermo-optic effect causes the refractive index of that medium to show variation with temperature. Temperature sensitivity can be calculated using the following equation:[32]

$$S_T = \frac{\Delta\lambda_{res}}{\Delta T} \tag{11}$$

where $\Delta T =$ the corresponding change in temperature. PDMS is chosen as the material held inside the LRC, offering numerous advantages over other such temperature-sensitive liquids. For example, PDMS possesses a large thermo-optic coefficient and also remains stable under varying environmental and pressure conditions as a solid and fireproof element.[33] The relation between the temperature and refractive index of PDMS is expressed using the following equation:[32]

$$n_{PDMS} = 1.4176 - 4.5 \times 10^{-4} \times T \tag{12}$$

where T is the temperature of the PDMS (in °C). With the rise in the value of T from 20 °C to 80 °C, the resonant peak of mode 1 undergoes a blueshift (Fig. 10(a and b)). The shift in the peak is linearly related to the temperature with a negative coefficient of correlation. The sensor exhibits a temperature sensitivity of 0.488 nm $°C^{-1}$.

The temperature detection limit (DL_T) represents the smallest change in temperature that the sensor can accurately detect. Its value can be determined by calculating the ratio of the smallest wavelength shift that can be perceived using an OSA to the sensor's temperature sensitivity:[27]

$$DL_T = \frac{\Delta\lambda_{min}}{S_T} \tag{13}$$

Using the measured temperature sensitivity of 0.488 nm $°C^{-1}$, the value of DL_T for the sensor is calculated to be 2.05×10^{-3} °C. With this minute level of detection limit, the device can sense extremely small temperature variations, enabling accurate measurement of subtle thermal changes.

As shown in Fig. 10(c), mode 2 (pressure-sensitive mode) remains invariant to the temperature variation of PDMS. The resonant wavelength for mode 2 remains fixed at 1712.6 nm as the temperature of the PDMS changes, confirming that the pressure-sensing mode is impervious to thermal variations. This result, together with the pressure-independence of mode 1 (Fig. 9(c)) confirms the independent crosstalk-free dual-sensing capability of both pressure and temperature in the proposed structure.

To evaluate the influence of thermal expansion on the resonance shift and potentially the device performance, we considered the Coefficient of Thermal Expansion (CTE) of both the gold and PDMS layers. Gold exhibits a relatively low CTE of approximately 14.2×10^{-6} $°C^{-1}$, whereas PDMS exhibits a significantly higher value of 310×10^{-6} $°C^{-1}$.[34,35]

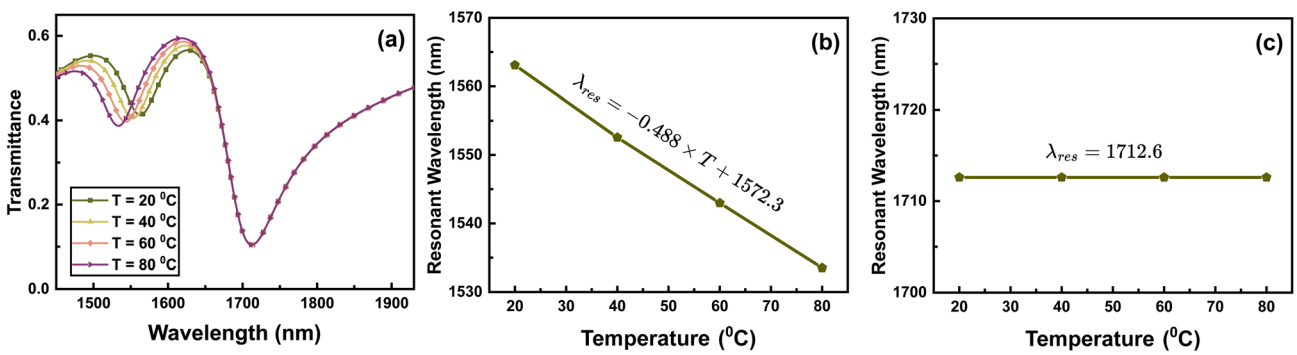

Fig. 10 (a) Transmittance profile of the proposed sensor under varying temperatures of PDMS. (b) Graph of resonant wavelength *versus* temperature for mode 1. (c) Graph of resonant wavelength *versus* temperature for mode 2.

© 2025 The Author(s). Published by the Royal Society of Chemistry

Open Access Article. Published on 09 October 2025. Downloaded on 1/29/2026 1:22:41 PM.
This article is licensed under a Creative Commons Attribution-NonCommercial 3.0 Unported Licence.

Over the operational temperature range from 20 °C (room temperature) up to 80 °C, the corresponding linear expansion of PDMS filling a rectangular cavity (with length $L_2 = 358$ nm) would be approximately 6.7 nm, equivalent to a relative change of ~1.9%. In contrast, the gold layer enclosing the PDMS in the RC would undergo an expansion of roughly 0.31 nm, with a percentage change of only ~0.09%. This expansion of gold is negligible compared to that of PDMS, and hence we can confidently state that the gold layer roughly stays the same in terms of geometry, with the PDMS layer mainly undergoing the expansion. However, the PDMS layer in our structure is enclosed within a rectangular cavity fenced by the gold structure, which constrains its ability to expand freely. Thus, the thermally induced expansion of PDMS leads to the development of compressive stress within the cavity.

Previous experimental investigations concerning the performance of PDMS layers experiencing mechanical stress have reported that such compressive stresses acting upon PDMS structures do not induce shifts in the wavelength of spectrum lines, but may cause minor changes in the magnitude of the coefficient of absorption of PDMS, as reported from its transmission characteristics.[36] This suggests that the thermal expansion mismatch does not compromise the spectral stability of the sensor, owing to the negligible thermal expansion of gold and the constrained expansion of PDMS. The resonance wavelength positions are expected to remain largely unaffected across the considered temperature range, ensuring robust performance under varying operational conditions.

Potential thermal hysteresis and optical drift in PDMS can also affect the long-term accuracy of the sensor. To investigate the impact of temperature-induced hysteresis on the sensor performance, we considered operating temperatures in the range of 40 °C to 80 °C. Experimental studies on thermal cycling involving heating and cooling of PDMS-based resonant structures for temperature monitoring report excellent repeatability and negligible hysteresis.[37] Across two full thermal cycles, the initial and final resonance wavelengths changed by at most 0.4 nm, corresponding to an equivalent temperature error of only ~2.23 °C over a 40 °C span. These data indicate that, within this temperature range, the contribution of thermal hysteresis to spectral uncertainty is on the sub-nanometer scale and does not severely affect sensing accuracy.[37] In line with these observations, our device is also operated in the same temperature window (≤80 °C); hence, our device is also expected to exhibit a hysteresis-induced shift of the resonant peak that remains below the sub-nanometer level over routine thermal cyclings. Consequently, thermal hysteresis has minimal impact on sensing accuracy in our operating temperature range.

Additionally, PDMS is also known to exhibit ageing-related optical drift, which can impact the long-term reliability of temperature sensing. During the repeated thermal cycles, residual stress accumulation may gradually alter the refractive index distribution, resulting in optical drift over time and progressively influencing the accuracy of the sensor over extended operation.[36,38] Although studies indicate minimal drift (change in the transmission spectrum) over months under ambient conditions, such drift can compromise accuracy in long-term sensing applications.[38] To address this, periodic recalibration against a known temperature reference or an *in situ* calibration method (a real-time reference) can be employed to correct the induced shift in the resonant peak due to optical drift. By adopting these strategies, the influence of optical drift over time can be effectively minimized, ensuring reliable operation of the sensor over an extended operational lifetime.

3.3 Dual-modal sensing of pressure and temperature

The integration of dual-modal sensing capability in the proposed sensor allows simultaneous and independent measurement of both pressure and temperature. This functionality is achieved because of the distinct modes associated with the two independent cavities (TTR and LRC) within the sensor structure. As discussed in Sections 3.1 and 3.2, the peak corresponding to mode 1 undergoes a blueshift when the temperature increases, whereas mode 2 witnesses a redshift corresponding to an increase in applied pressure at the top horizontal slot of the TTR. Since mode 1 is not affected by the change in pressure and mode 2 is free from the effect of temperature change, this allows us to concurrently detect both pressure and temperature independently.

Fig. 11(a) illustrates the transmittance profile of the sensor while acting as a dual-function sensor for simultaneous

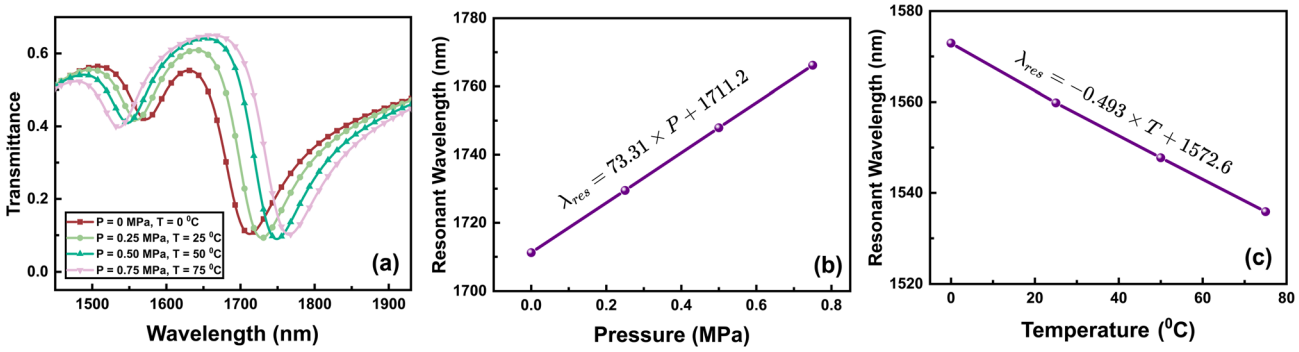

Fig. 11 (a) Transmission profile of the proposed sensor while performing dual-sensing under different pressures and temperatures. (b) Resonant wavelength *versus* pressure for mode 2. (c) Resonant wavelength *versus* temperature for mode 1.

Open Access Article. Published on 09 October 2025. Downloaded on 1/29/2026 1:22:41 PM. This article is licensed under a Creative Commons Attribution-NonCommercial 3.0 Unported Licence.

detection of temperature and pressure. The pressure applied is increased from 0 MPa to 0.75 MPa in steps of 0.25 MPa, while the temperature is varied from 0 °C to 75 °C in steps of 25 °C. It is observed that the conclusion drawn from the previous transmission profiles (Fig. 9(a) and 10(a)) still persists when performing simultaneous sensing of both parameters. When there is an increase in the temperature of the PDMS held in the LRC, as well as in the pressure applied at the top, mode 1 and mode 2 undergo a blueshift and redshift, respectively.

Building upon the observations in Sections 3.1 and 3.2, where the transmission peaks at mode 1 and mode 2 were found to be insensitive to variations in pressure and temperature, respectively, we further investigated the independence of the two sensing channels during dual sensing. The sensitivities of mode 1 (temperature) and mode 2 (pressure) were calculated during simultaneous variation of both parameters. Fig. 11(b and c) show that the pressure sensitivity obtained from the resonant peak at mode 2 during dual sensing was 73.31 nm MPa^{-1}, while the temperature sensitivity recorded from mode 1 was 0.493 nm $°C^{-1}$. The deviations in sensitivity from their nominal value were minimal, with only ~4.9% for pressure and ~1% for temperature, confirming that the interaction between the channels is negligible. These small variations indicate that the modes operate largely independently, supporting the crosstalk-free behavior of the proposed sensor.

Finally, a comparison of our proposed sensor is made with state-of-the-art works conducted on MIM-based optical pressure sensors in Table 3. From the presented table, it is clear that all the works conducted until now have primarily focused on improving the sensor's sensitivity. None of the research deals with the problem of oxidation, which can heavily impact the performance of their sensor while functioning in a real-world setting. Metallic thin films, such as silver, experience deterioration of their optical properties when they are exposed to air. This leads to the formation of clumps of silver sulfide on their surface, which further experience an increase in the nucleation site density and clustering. In contrast, the use of gold in our work ensures that the sensor benefits from having an extended lifetime and stability while being used under extreme conditions such as humid or corrosive environments. Moreover, dual sensing capability among sensors has been gaining popularity recently. This special feature is present in our sensor, which showcases its versatile nature and applicability across various practical fields.

4 Material choice trade-offs

The preceding section highlights the optical performance of our sensor design; besides this, it is also important for us to take into account the practical trade-offs associated with the use of gold in our sensor design. While gold's chemical and optical stability are major benefits, it comes at the expense of a higher material cost compared to silver. This makes it incumbent upon us to control the use of gold-based sensors for disposable or large-volume applications, considering the economic feasibility in the case of large-scale production. For this reason, we envision our sensor being most suitable for scenarios where long-term performance, reliability, and resistance to environmental degradation are critical. These include applications in aerospace systems, industrial monitoring, biomedical diagnostics, or other high-value applications that justify the investment in durable materials.

To provide a more comprehensive evaluation, we quantitatively evaluated gold and silver across several performance metrics. Firstly, we compared the real and imaginary parts of the permittivity of gold and silver, as shown in Fig. 12(a and b).

We observe that in the visible spectrum, both the real and imaginary permittivity of gold and silver share an overlap. As we reach the Near-Infrared (NIR) region, the real part of gold's permittivity tends to be slightly more negative than that of silver. The real part of the permittivity determines the strength of plasmonic confinement, with a more negative real permittivity indicating a greater confinement of the evanescent field at the metal–dielectric juncture for the case of gold. On the other hand, the imaginary part governs the material's intrinsic optical losses, where a higher imaginary permittivity leads to greater losses and reduced absorption.[6,43] From Fig. 12(b), we observe that the imaginary permittivity for gold exceeds that for silver in the NIR region of the electromagnetic spectrum, indicating that gold endures a higher intrinsic optical loss.

To investigate these implications further, we calculated the quality factor (Q_{SPP}) and propagation length of (δ_{SPP}) of the SPPs for both metals. The quality factor of the SPP incorporates both the field confinement (linked to the real permittivity) and the loss (linked to the imaginary permittivity) using the formula $Q_{SPP} = \mathrm{Re}(\varepsilon)^2/\mathrm{Im}(\varepsilon)$, where $\mathrm{Re}(\varepsilon)$ and $\mathrm{Im}(\varepsilon)$ represent the real and imaginary permittivity of the metal (gold or silver), respectively.[44,45] The comparative analysis of the Q_{SPP} for both gold and silver is depicted in Fig. 12(c). The propagation length is

Table 3 Comparative analysis with existing literature on MIM-based optical pressure sensors

Reference	Material	Pressure sensitivity (nm MPa^{-1})	Temperature sensitivity (nm $°C^{-1}$)	Oxidation problem	Dual sensing
16	Ag	25.4	—	Present	×
39	Ag	16.5	—	Present	×
11	Si	51.075	—	Present	×
40	Ag	—	0.4	Present	×
41	Ag	—	0.225	Present	×
42	Ag	12.48	0.36	Present	✓
This work	Au	77.1	0.488	Absent	✓

© 2025 The Author(s). Published by the Royal Society of Chemistry

Open Access Article. Published on 09 October 2025. Downloaded on 1/29/2026 1:22:41 PM.
This article is licensed under a Creative Commons Attribution-NonCommercial 3.0 Unported Licence.

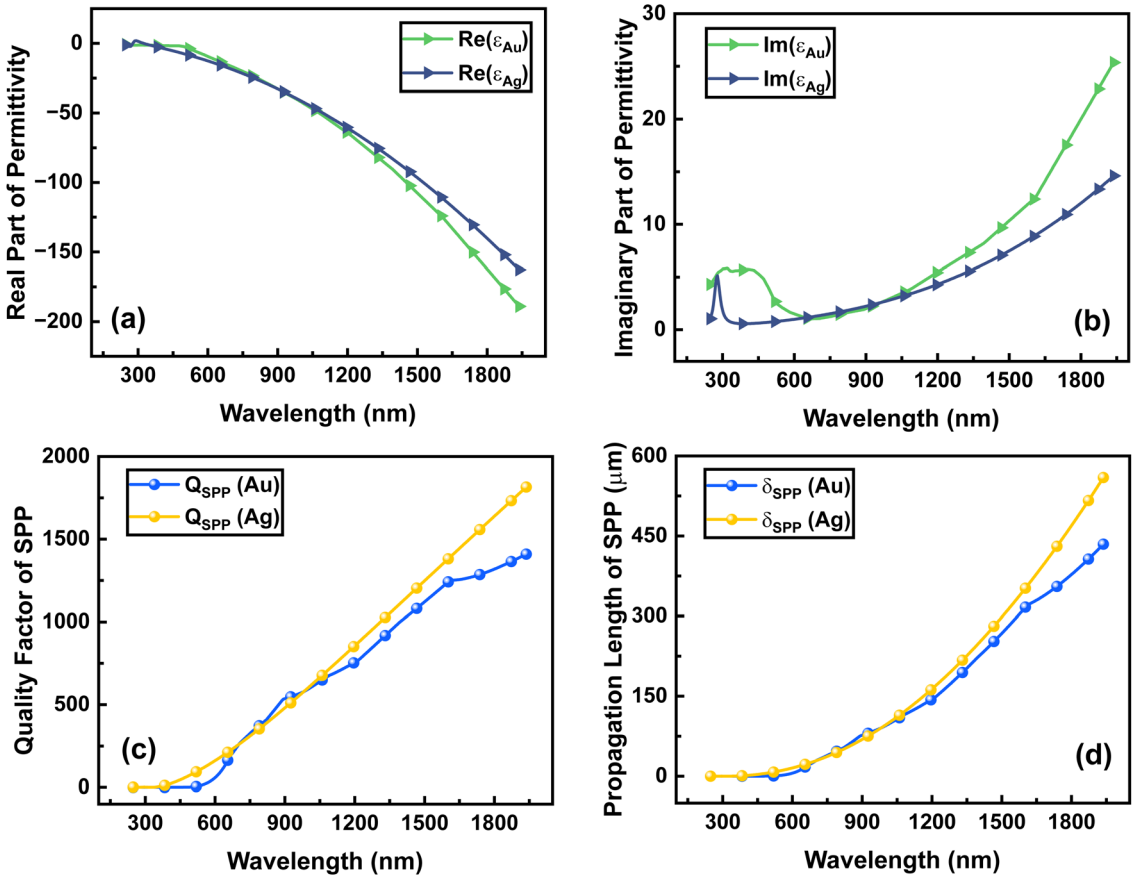

Fig. 12 Comparison of (a) real permittivity, (b) imaginary permittivity, (c) quality factor of the SPP, and (d) propagation length of the SPP among gold and silver.

analyzed using the formula $\delta_{SPP} = \frac{\lambda_0}{2\pi}(\mathrm{Re}(\varepsilon)^2/\mathrm{Im}(\varepsilon))$. δ_{SPP} quantifies how far an SPP mode can travel along the metal–dielectric interface, serving as a direct indicator of loss performance.[46] Fig. 12(d) compares the value of δ_{SPP} between gold and silver.

From Fig. 12(c), it is evident that silver exhibits a consistently higher Q_{SPP} than gold across most of the measured wavelength range, confirming its lower intrinsic losses. This advantage is particularly pronounced in the NIR region, where the imaginary permittivity difference between the two metals is largest. Similarly, Fig. 12(d) shows that the δ_{SPP} for silver exceeds that of gold in the NIR region. This extended propagation capability does indicate reduced damping in silver, but if we meticulously observe the graphs, we see that the difference in the value of Q_{SPP} and δ_{SPP} is more pronounced at higher wavelengths. In contrast, at shorter wavelengths, their magnitudes mostly overlap.

Motivated by these observations, a further numerical investigation was conducted by replacing gold with silver in our proposed sensor design. This allowed for direct assessment of how the intrinsic material advantages of silver, indicated by higher Q_{SPP} and longer δ_{SPP} in the NIR, translate into practical device-level performance. The transmission characteristics obtained while using silver as the material in place of gold and applying the device as a pressure and temperature sensor are presented in Fig. 13 and 14, respectively.

Key performance metrics, including the quality factor of the resonant modes, pressure and temperature sensitivity for the structure with silver incorporated, were evaluated. The quality factor for each of the modes is determined using the formula, $Q\text{-factor} = \frac{\lambda_{res}}{\mathrm{FWHM}}$, where FWHM represents the full width at half maximum for the corresponding resonant peak.[47] The results of the investigation are summarized in Table 4.

Despite silver's superior intrinsic plasmonic properties (Q_{SPP} and δ_{SPP}), the overall sensor performance did not show a significant improvement compared to the gold-based design. In fact, gold demonstrated a slightly higher quality factor for mode 2 and an enhanced pressure sensitivity, particularly in the NIR region relevant to our application. This outcome can be attributed to gold's better field confinement resulting from a more negative real permittivity, which helps it to overcome the losses and thus show better resonance characteristics than silver during practical applications. As a result, despite the fact that silver offers theoretical advantages in terms of lower loss and longer SPP propagation, gold remains the preferred material choice for our sensor due to its superior performance in key sensing metrics, combined with its chemical stability and long-term reliability.

© 2025 The Author(s). Published by the Royal Society of Chemistry

Open Access Article. Published on 09 October 2025. Downloaded on 1/29/2026 1:22:41 PM.
This article is licensed under a Creative Commons Attribution-NonCommercial 3.0 Unported Licence.

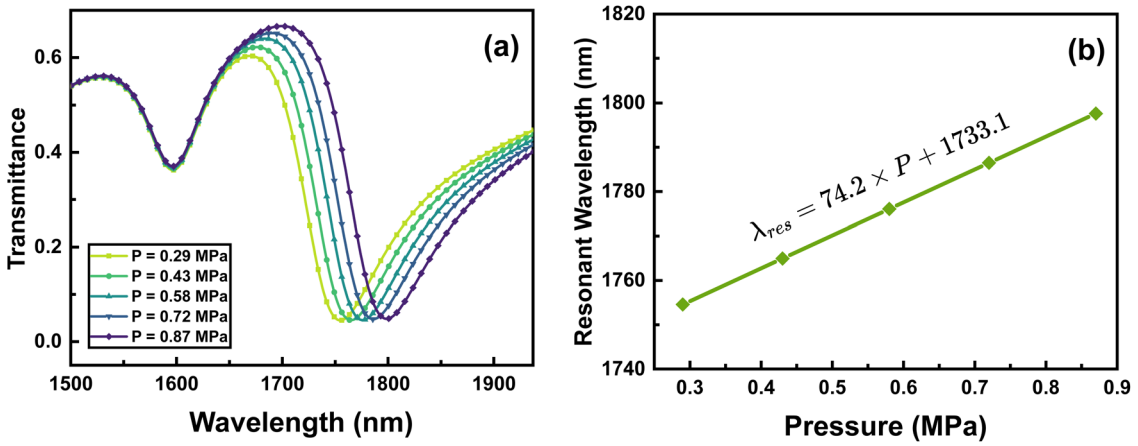

Fig. 13 (a) Transmittance profile of the proposed sensor with silver incorporated, under varying applied pressure. (b) Graph of resonant wavelength *versus* pressure for mode 2.

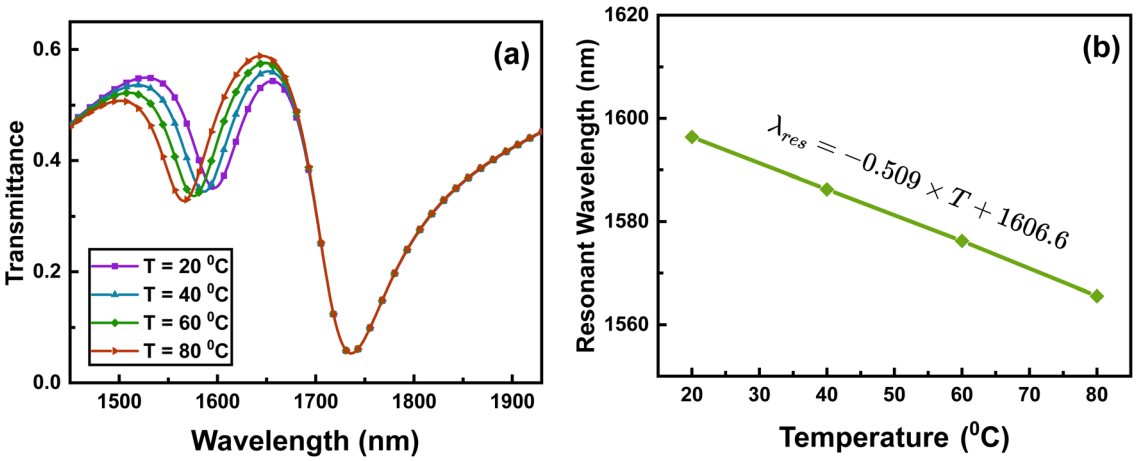

Fig. 14 (a) Transmittance profile of the proposed sensor with silver incorporated, under varying temperatures of PDMS. (b) Graph of resonant wavelength *versus* temperature for mode 1.

5 Fabrication of the proposed sensor

We have presented a complete fabrication process in this section to illustrate the feasibility of practically realizing the sensor prototype in future work. The proposed sensor can be fabricated using soft UV nanoimprint lithography (UV-NIL). Soft UV-NIL facilitates large-scale production on a full wafer in one step at room temperature and low pressure.[48] This method is cost-effective and highly efficient, making it suitable for fabricating micro- and nanoscale devices. The fabrication steps are illustrated in Fig. 15.

Table 4 Qualitative and quantitative comparison of gold- and silver-based design of the proposed sensor

Metric	Gold (Au)	Silver (Ag)	Performance difference
Real part of the permittivity	More negative in the NIR range	Less negative in the NIR	Au supports tighter mode confinement
Imaginary part of the permittivity	Slightly higher in the NIR	Lower in the NIR	Ag exhibits lower optical loss
SPP quality factor	Slightly lower in the NIR	Slightly higher in the NIR	Ag has a better SPP quality factor
SPP propagation length	Shorter in the NIR	Longer in the NIR	Ag enables longer-range SPP
Pressure sensitivity	77.1 nm MPa^{-1}	74.2 nm MPa^{-1}	Au offers higher spectral shift
Temperature sensitivity	0.488 nm $°C^{-1}$	0.509 nm $°C^{-1}$	Almost equal spectral shift
Quality factor of mode 1	32.8	33.1	Almost equal
Quality factor of mode 2	16.2	15.2	Higher for Au
Material cost	Higher	Lower	Ag is more economical
Chemical stability	Excellent (resists oxidation)	Poor (prone to oxidation)	Au preferred

© 2025 The Author(s). Published by the Royal Society of Chemistry

Open Access Article. Published on 09 October 2025. Downloaded on 1/29/2026 1:22:41 PM. This article is licensed under a Creative Commons Attribution-NonCommercial 3.0 Unported Licence.

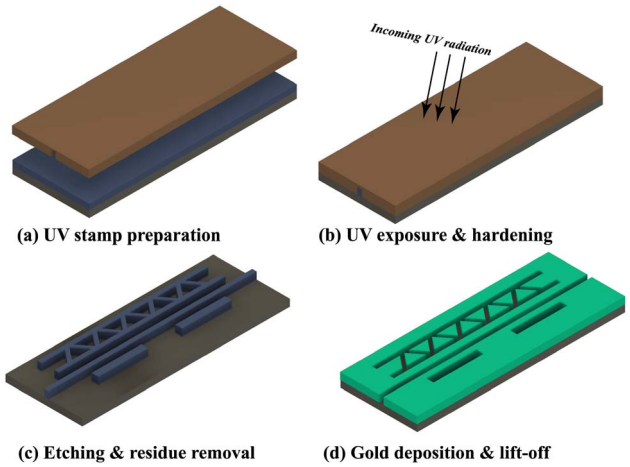

Fig. 15 Fabrication procedure for the proposed dual-function optical sensor.

In the first stage of fabrication, Electron Beam Lithography (EBL) is used to define patterns on a polymethylmethacrylate (PMMA) resist applied to a silicon substrate. The pattern is etched into the silicon wafer using Reactive Ion Etching (RIE), and the PMMA is subsequently removed.[49,50] Afterwards, a layer of hard polydimethylsiloxane (H-PDMS) is spin-coated onto the silicon master mold, which is pre-treated with trimethylchlorosilane (TMCS) to prevent sticking.[50] To ensure flexibility, a layer of standard PDMS is applied over the hard PDMS layer.[50] The bilayer stamp is carefully detached and cured from the silicon master mold.[49] The stamp is used to imprint the design onto a UV-curable resist such as AMONIL, which is spin-coated over a sacrificial PMMA layer. The stamp is pressed onto the resist to perform this task. In the subsequent stage, the patterned resist is hardened by UV exposure at a wavelength of 365 nm under controlled energy and pressure.[51] The residual resist is eliminated using RIE. In the final step of fabrication, a chromium adhesion layer is deposited, followed by gold deposition under vacuum conditions using electron beam evaporation.[51]

6 Conclusion

In this article, we propose a dual-function optical pressure sensor based on the MIM waveguide configuration, which consists of a triangular truss resonator and a pair of rectangular cavities, utilizing oxidation-resistant gold as the plasmonic material. COMSOL Multiphysics software is used to numerically compute the transmission characteristics of the device's 2D layout. The sensor demonstrates exceptional performance, accomplishing pressure and temperature sensitivities of 77.1 nm MPa^{-1} and 0.488 nm $°C^{-1}$, respectively. This study not only addresses the limitations of traditional plasmonic materials such as silver, but also pioneers the development of sensing platforms capable of weathering real-world challenges. Its quantitative performance, robustness and ability to operate under extreme environmental conditions accentuate its potential for implementation in cutting-edge optical and mechanical sensing technologies.

Author contributions

Abdullah Taharat: conceptualization, investigation, methodology, visualization, software, writing – original draft. Mohammad Abrar Kabir: formal analysis, methodology, visualization, software, writing – original draft. Aseer Imad Keats: investigation, visualization, software, writing – original draft. A. K. M. Rakib: methodology, writing – review & editing, project administration, supervision. Rakibul Hasan Sagor: writing – review & editing, project administration, supervision.

Conflicts of interest

There are no conflicts to declare.

Data availability

The data supporting the findings of this study are available within the article. No additional data were generated or analyzed in the presented research.

Acknowledgements

The authors express their gratitude to the Islamic University of Technology for its support and encouragement in conducting this research.

References

1 W. L. Barnes, A. Dereux and T. W. Ebbesen, *Nature*, 2003, **424**, 824–830.
2 J. Zhang, L. Zhang and W. Xu, *J. Phys. D: Appl. Phys.*, 2012, **45**, 113001.
3 A. V. Zayats, I. I. Smolyaninov and A. A. Maradudin, *Phys. Rep.*, 2005, **408**, 131–314.
4 Y.-F. Chau, H.-H. Yeh and D. Tsai, *J. Electromagn. Waves Appl.*, 2010, **24**, 1005–1014.
5 E. Forati and G. W. Hanson, *Appl. Phys. Lett.*, 2013, **103**, 133104.
6 M. A. Kabir, A. Taharat, A. I. Keats, A. Rakib, M. Z. A. Rony and R. H. Sagor, *Opt. Express*, 2025, **33**, 19788–19809.
7 M. R. Rakhshani and M. A. Mansouri-Birjandi, *Sens. Actuators, B*, 2017, **249**, 168–176.
8 T. Intisar, A. S. Alam, I. Hoque and M. O. Faruque, *Heliyon*, 2024, **10**, e26186.
9 Y.-J. Guo, K.-D. Xu, X. Deng, X. Cheng and Q. Chen, *IEEE Electron Device Lett.*, 2020, **41**, 1165–1168.
10 M. A. Butt, *Appl. Sci.*, 2024, **14**, 4714.
11 A. Taharat, M. A. Kabir, A. I. Keats, A. Rakib and R. H. Sagor, *Opt. Commun.*, 2025, **578**, 131495.
12 S. Upadhyay, V. L. Kalyani and C. Charan, *Proceedings of International Conference on ICT for Sustainable Development: ICT4SD*, 2016, vol 1, pp. 269–278.
13 Y. Fang and M. Sun, *Light: Sci. Appl.*, 2015, **4**, e294.

© 2025 The Author(s). Published by the Royal Society of Chemistry

Open Access Article. Published on 09 October 2025. Downloaded on 1/29/2026 1:22:41 PM. This article is licensed under a Creative Commons Attribution-NonCommercial 3.0 Unported Licence.

14 B.-H. Zhang, L.-L. Wang, H.-J. Li, X. Zhai and S.-X. Xia, *J. Opt.*, 2016, **18**, 065001.
15 J. Wu, P. Lang, X. Chen and R. Zhang, *J. Mod. Opt.*, 2015, **63**, 219–223.
16 I. Tathfif, A. A. Yaseer, K. S. Rashid and R. H. Sagor, *Opt. Express*, 2021, **29**, 32365–32376.
17 X. Ma, T. Li, Y. Wang and Z. Chen, *Plasmonics*, 2024, 1–8.
18 H. Bennett, R. Peck, D. Burge and J. Bennett, *J. Appl. Phys.*, 1969, **40**, 3351–3360.
19 P. B. Johnson and R.-W. Christy, *Phys. Rev. B: Condens. Matter Mater. Phys.*, 1972, **6**, 4370.
20 S. Maier, *Plasmonics: Fundamentals and Applications*, 2007.
21 M. Danaie and A. Shahzadi, *Plasmonics*, 2019, **14**, 1453–1465.
22 F. Hu, H. Yi and Z. Zhou, *Opt. Express*, 2011, **19**, 4848–4855.
23 F. Ma and X. Liu, *Appl. Opt.*, 2007, **46**, 6247–6250.
24 J. Dionne, L. Sweatlock, H. Atwater and A. Polman, *Phys. Rev. B: Condens. Matter Mater. Phys.*, 2006, **73**, 035407.
25 G. Duan, P. Lang, L. Wang, L. Yu and J. Xiao, *Mod. Phys. Lett. B*, 2016, **30**, 1650284.
26 M. Salvadori, I. Brown, A. Vaz, L. Melo and M. Cattani, *Phys. Rev. B: Condens. Matter Mater. Phys.*, 2003, **67**, 153404.
27 T. T. Treena, M. A. Karim and N. M. Munim, *Opt. Express*, 2025, **33**, 4662–4681.
28 K. V. Voronin, Y. V. Stebunov, A. A. Voronov, A. V. Arsenin and V. S. Volkov, *Sensors*, 2019, **20**, 203.
29 C.-W. Baek, J.-M. Kim, Y.-K. Kim, J. H. Kim, H. J. Lee and S. W. Han, *Sens. Mater.*, 2005, **17**, 277–288.
30 B. Merle and M. Göken, *J. Mater. Res.*, 2014, **29**, 267–276.
31 Y.-X. Huang, Y.-Y. Xie, W.-L. Zhao, H.-J. Che, W.-H. Xu, X. Li and J.-C. Li, *IEEE 20th International Conference on Embedded and Real-Time Computing Systems and Applications*, 2014, pp. 1–5.
32 M. F. Hassan, R. H. Sagor, I. Tathfif, K. S. Rashid and M. Radoan, *IEEE Sens. J.*, 2020, **21**, 1461–1469.
33 J. Zhu and J. Lou, *Results Phys.*, 2020, **18**, 103183.
34 A. Oliva, J. Lugo, R. Gurubel-Gonzalez, R. Centeno, J. Corona and F. Avilés, *Thin Solid Films*, 2017, **623**, 84–89.
35 A. Müller, M. C. Wapler and U. Wallrabe, *Soft Matter*, 2019, **15**, 779–784.
36 I. Turek, N. Tarjányi, I. Martinček and D. Káčik, *Opt. Mater.*, 2014, **36**, 965–970.
37 D. Yi, Z. Huo, Y. Geng, X. Li and X. Hong, *Opt. Fiber Technol.*, 2020, **57**, 102185.
38 C. A. Zimmermann, K. N. Amouzou and B. Ung, *Adv. Opt. Mater.*, 2025, **13**, 2401975.
39 P. Palizvan, S. Olyaee and M. Seifouri, *Photonic Sens.*, 2018, **8**, 242–247.
40 F. Chen and W. Yang, *J. Opt. Soc. Am. B*, 2023, **40**, 736–742.
41 F. Chen and J. Li, *Mod. Phys. Lett. B*, 2019, **33**, 1950017.
42 X. Zhang, H. Tian, Y. Liu and J. Song, *Appl. Opt.*, 2023, **62**, 6771–6778.
43 A. S. Souza, V. Coelho and J. L. O. Santos, *Braz. J. Phys.*, 2021, **51**, 449–460.
44 M. G. Blaber, M. D. Arnold and M. J. Ford, *J. Phys.: Condens. Matter*, 2010, **22**, 143201.
45 M. G. Blaber, M. D. Arnold and M. J. Ford, *J. Phys.: Condens. Matter*, 2010, **22**, 095501.
46 W. L. Barnes, *J. Opt. Pure Appl. Opt.*, 2006, **8**, S87.
47 R. Al Mahmud, M. O. Faruque and R. H. Sagor, *Plasmonics*, 2021, **16**, 873–880.
48 U. Plachetka, M. Bender, A. Fuchs, B. Vratzov, T. Glinsner, F. Lindner and H. Kurz, *Microelectron. Eng.*, 2004, **73**, 167–171.
49 A. Cattoni, J. Chen, D. Decanini, J. Shi and A.-M. Haghiri-Gosnet, *Recent Advances in Nanofabrication Techniques and Applications*, 2011, pp. 139–156.
50 G. Barbillon, F. Hamouda, S. Held, P. Gogol and B. Bartenlian, *Microelectron. Eng.*, 2010, **87**, 1001–1004.
51 J.-F. Bryche, F. Hamouda, M. Besbes, P. Gogol, J. Moreau, M. L. de la Chapelle, M. Canva and B. Bartenlian, *Micro Nano Eng.*, 2019, **2**, 122–130.

© 2025 The Author(s). Published by the Royal Society of Chemistry